

LETTER TO THE EDITOR

High speed stars: III. Detailed abundances and binary nature of the extreme speed star GHS143 ★ ★★

E. Caffau¹, P. Bonifacio¹, L. Monaco², L. Sbordone³, M. Spite¹, P. François^{4,5}, P. Panuzzo¹, P. Sartoretti¹, L. Chemin⁶,
F. Thévenin⁷, and A. Mucciarelli⁸

¹ GEPI, Observatoire de Paris, Université PSL, CNRS, 5 Place Jules Janssen, 92190 Meudon, France

² Universidad Andres Bello, Facultad de Ciencias Exactas, Departamento de Ciencias Físicas - Instituto de Astrofísica, Autopista Concepción-Talcahuano, 7100, Talcahuano, Chile

³ European Southern Observatory, Casilla 19001, Santiago, Chile

⁴ GEPI, Observatoire de Paris, Université PSL, CNRS, 77 Av. Dendert-Rocheau, 75014 Paris, France

⁵ UPJV, Université de Picardie Jules Verne, 33 rue St Leu, 80080 Amiens, France

⁶ Universidad Andres Bello, Facultad de Ciencias Exactas, Departamento de Ciencias Físicas - Instituto de Astrofísica, Fernandez Concha 700, Las Condes, Santiago, Chile

⁷ Université de Nice Sophia-Antipolis, CNRS, Observatoire de la Côte d'Azur, Laboratoire Lagrange, BP 4229, F-06304 Nice, France

⁸ Dipartimento di Fisica e Astronomia, Università degli Studi di Bologna, Via Gobetti 93/2, I-40129 Bologna, Italy

Received September 15, 1996; accepted March 16, 1997

ABSTRACT

Context. The Gaia satellite has provided the community with three releases containing astrometrical and photometric data as well as by products, such as stellar parameters and variability indicators.

Aims. By selecting in the Gaia database, one can select stars with the requested characteristics, such as high speed. At present any selection is based on available Gaia releases including a subset of the observations. This, for some stars, can show some limitations, for example there is still not a sufficient number of observations to detect binarity.

Methods. We investigated a star selected in Gaia EDR3 for its high speed that appears unbound to the Galaxy. We requested high-quality spectra to derive more information on the star.

Results. From the spectroscopic investigation we confirm the low metallicity content of the star, and we derive a detailed chemical composition. The star is poor in carbon and very rich in oxygen: $[(C+N+O)/Fe]=+0.65$. From the two spectra observed we conclude that the star is in a binary system and from the investigation of the ionisation balance we derive that the star is closer than implied by the Gaia DR3 parallax, and thus has a lower intrinsic luminosity.

Conclusions. The star is probably still unbound, but there is the possibility that it is bound to the Galaxy. Its low carbon abundance suggests that the star was formed in a dwarf galaxy.

Key words. Stars: abundances - Galaxy: abundances - Galaxy: evolution - Galaxy: formation

1. Introduction

In an ongoing investigation, we are trying to characterise the population of stars with high speed with respect to the Sun. In Caffau et al. (2020b, hereafter Paper I), we selected in Gaia Data Release 2 (DR2) (Gaia Collaboration et al. 2018) a sample of 72 stars for their high transverse velocity ($V_{\text{trans}} > 500 \text{ km s}^{-1}$). In the sample, we highlighted a few apparently young stars, according to their position in the Gaia colour–absolute magnitude diagram. The sample was further discussed in Bonifacio et al. (2024, hereafter Paper II), where two other samples, selected with the same criterion on V_{trans} in Gaia EDR3 (Gaia Collaboration et al. 2022), are analysed. In Paper II other seemingly young metal-poor stars are detected and discussed. In particular, GHS143 (Gaia DR3 6632370485122299776) is a metal-poor

evolved star of G magnitude 13.06 and of apparent young age, characterised by extreme kinematics. Assuming the parallax, proper motions, and radial velocity in Gaia DR3 (Gaia Collaboration et al. 2022), it can be seen that GHS143 is not bound to the Galaxy, but is falling into it. We requested high-resolution spectra of this star to investigate if the stellar parameters we derived from a high-resolution spectrum are consistent with the Gaia DR3 parallax and photometry, and also to check for possible radial velocity variations. In this paper we use these spectra to derive a complete chemical inventory of this star, derive the uncertainties, and discuss the possibility that the star is bound to the Galaxy.

2. Observations

Two UVES (Dekker et al. 2000) spectra have been secured for this star. In the ESO programme 111.22EH.001 the star was observed on August 20, 2023, in the setting DIC2 437+760 (wave-

* Based on observations made with UVES at VLT 111.24J1.001 and 112.25EH.001.

** The lines investigated are on an on-line table at CDS.

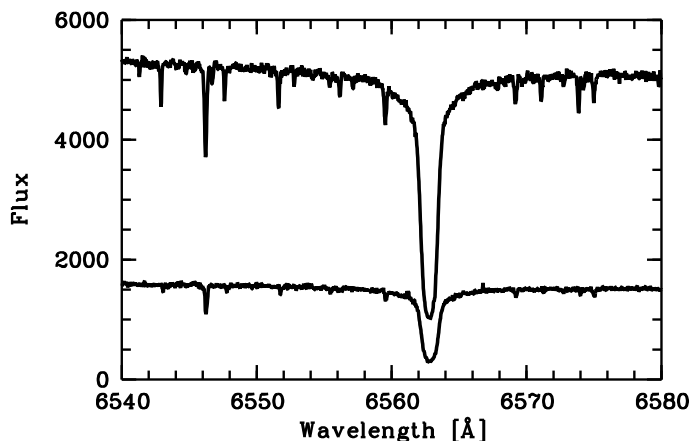


Fig. 1. Observed spectra in the $H\alpha$ region. The spectrum with higher flux is from November 2023; the lower flux is from August 2023.

length ranges 373–499 and 565–946 nm), with slit $0''.4$ (resolving power 90 000) in the blue arm and $0''.3$ (resolving power 110 000) in the red arm. In the ESO programme 0112.25EH.001 the star was observed on November 11, 2023, with the same setting and with slit $0''.5$ (resolving power 75 000) in the blue arm and in the red arm. Both observations were graded ‘A’. The signal-to-noise ratio of the November spectrum is better than the August spectrum (S/N of 53 and 35 at 400 nm; 79 and 49 at 498 nm; 97 and 72 at 640 nm; 86 and 67 at 838 nm). We reduced the spectra using the ESO UVES pipeline. In Fig. 1 the two UVES spectra in the $H\alpha$ region are shown.

3. Analysis

3.1. Radial velocity

We used template matching to measure the radial velocities from the observed spectra. As a template we used a synthetic spectrum with the parameters derived in Bonifacio et al. (2024). The spectra were corrected for the barycentric Earth velocity using the value in the descriptor ESO.QC.VRAD.BARYCOR available in the reduced spectrum. We measured a radial velocity for each of the spectra collected in the three UVES detectors (one in the blue arm and two in the red arm). We used the following wavelength ranges: 376 nm–497 nm for the blue arm, 570 nm–676 nm for the lower detector of the red arm, and 800 nm–900 nm for the upper detector of the red arm. We then adopted the mean of these three measurements as the radial velocity and the standard deviation of the three values as an estimate of the error on the radial velocity. From the UVES spectrum of August 2023 we derived a V_r of $22.71 \pm 0.30 \text{ km s}^{-1}$ and from the spectrum of November 2023 a V_r of $25.58 \pm 0.40 \text{ km s}^{-1}$, to be compared to the Gaia DR3 V_r of $17.5 \pm 1.64 \text{ km s}^{-1}$. From these three values it is clear that the star displays radial velocity variations that make it likely that the star belongs to a multiple system. We add that the radial velocity measured on the low-resolution spectrum discussed in Paper II is $-27.7 \pm 4.0 \text{ km s}^{-1}$, where the error estimate is purely statistical. The spectrum was taken with FORS, which is subject to flexures, and the systematic error in radial velocity is 48.7 km s^{-1} , estimated as in Caffau et al. (2020a). Even so, this measurement, at face value, supports the existence of radial velocity variations in this star. A monitoring of its radial velocity, beyond what is available from the epoch radial velocities that are provided by Gaia, is strongly encouraged.

3.2. Stellar parameters

The star was analysed in Paper II and the stellar parameters adopted were $T_{\text{eff}}=5159 \text{ K}$, $\log g=1.8 \text{ dex}$, a microturbulence $\xi = 1.96 \text{ km s}^{-1}$; and an iron abundance of $[\text{Fe}/\text{H}] = -1.74 \text{ dex}$ was then derived. When adopting these stellar parameters to analyse the UVES spectra, we obtain Fe abundances in very good agreement ($[\text{Fe}/\text{H}] = -1.86 \pm 0.10 \text{ dex}$ and $[\text{Fe}/\text{H}] = -1.85 \pm 0.10 \text{ dex}$ from the two spectra), and in both cases a good Fe ionisation balance.

We allowed MyGIsFOS to derive the parameters and we obtained for T_{eff} , $\log g$, ξ , and $[\text{Fe}/\text{H}]$: 4988 ± 96 , 1.37 ± 0.05 , 1.59 ± 0.07 , and -1.92 ± 0.10 from the spectrum of August and 4956 ± 93 , 1.40 ± 0.07 , 1.54 ± 0.08 , and -1.95 ± 0.12 from the spectrum of November. The two spectra provide very coherent results. We used the calibration suggested by Frebel et al. (2013) to bring the effective temperature derived by the excitation on the photometric scale. With this calibration we derived 5159 and 5127 K, respectively, in excellent agreement with the value derived from the Gaia DR3 photometry and applied in Paper II. By using the calibration by Mucciarelli & Bonifacio (2020) to derive T_{eff} on the photometric scale of González Hernández & Bonifacio (2009), we derived 5136 and 5112 K, respectively, with an uncertainty of 130 K. We adopted $T_{\text{eff}}=5160 \text{ K}$.

To derive the stellar parameters we focused on the spectrum from November 2023, which has a higher flux, and to derive the uncertainties we used the August 2023 spectrum. We are aware that the Fe abundance derived from Fe I lines is affected by departure from local thermodynamical equilibrium (hereafter NLTE, the local thermodynamical equilibrium shall be referred to as LTE) and forcing the ionisation equilibrium does not take into account the NLTE effects. The NLTE correction we expect for this star is about 0.1 dex. We selected the Fe I lines retained by MyGIsFOS and also available from the web site of MPIA,¹ and with these 39 Fe I lines (providing $[\text{Fe}/\text{H}] = -1.76$) we derived the NLTE corrections (Bergemann et al. 2012b). For a sample of 30 Fe I lines with NLTE corrections from (Bergemann et al. 2012b), we verified the NLTE corrections as $\langle 3D \rangle_{\text{NLTE}} - 1D_{\text{LTE}}$ in Amarsi et al. (2016) and, with exactly the same stellar parameters, the average difference is 0.02 dex. We gave as input to MyGIsFOS several $\log g$ values (see Fig. 2) with fixed T_{eff} ; we derived the best agreement in $[\text{Fe}/\text{H}]$ from the Fe I and Fe II lines for $\log g = 2.1 \text{ dex}$. The NLTE correction is of 0.11 dex for $\log g = 2.1$ and spans values from 0.08 dex for the highest surface gravity to 0.13 dex for the lowest. These corrections are applied in Fig. 2. With fixed effective temperature and assuming LTE, the iron ionisation balance implies $\log g = 1.8$, as expected, lower than the value implied by the NLTE iron abundances.

We fixed T_{eff} and $\log g$ to derive the microturbulence and derived $1.65 \pm 0.07 \text{ km s}^{-1}$, changing very little by changing $\log g$ (a change of 0.02 km s^{-1} for a variation of 0.4 dex in $\log g$). The microturbulence derived by using the calibration of Mashonkina et al. (2017), with $T_{\text{eff}}=5159 \text{ K}$ and $\log g=2.1 \text{ dex}$, provided 1.83 km s^{-1} .

By assuming $T_{\text{eff}}=5159 \text{ K}$, $\log g=2.1 \text{ dex}$, and $\xi = 1.65 \text{ km s}^{-1}$, as derived by MyGIsFOS, we derived $[\text{Fe}/\text{H}]$ of -1.81 ± 0.11 and -1.70 ± 0.11 , when derived from Fe I and Fe II lines, respectively, in perfect agreement if we expect an NLTE correction of 0.11 dex (Bergemann et al. 2012b) on $[\text{Fe}/\text{H}]$ from Fe neutral lines. In Fig. 2 we show how the iron abundance derived from Fe I and Fe II lines changes, as a function of the adopted $\log g$. All values of surface gravity in the range 1.8–2.5 are acceptable, considering the involved uncertainties.

¹ https://nlte.mpia.de/gui-siuAC_secE.php

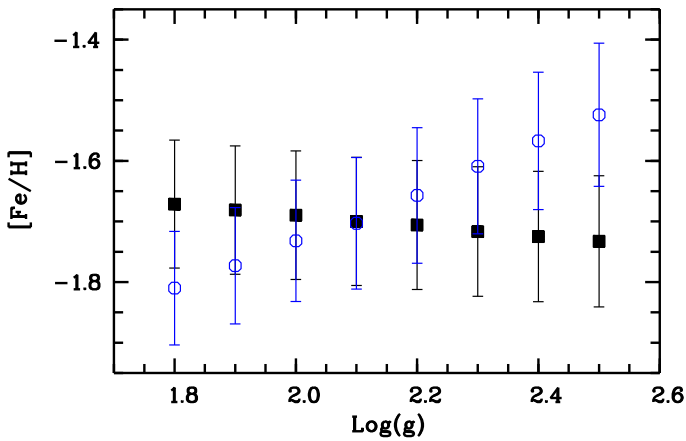


Fig. 2. $[\text{Fe}/\text{H}]$ derived from Fe I (filled black squares) and corrected by NLTE and from Fe II (blue open circles) lines vs $\log g$.

3.3. Stellar mass

In Paper II, we adopted the parallax provided in Gaia DR3 corrected by the zero-point (Lindegren et al. 2021), and we derived a mass of $3.1 M_{\odot}$ or $3.8 M_{\odot}$. According to the Fe ionisation balance, from the UVES spectra, we favour a higher $\log g$ that would imply that the star has a lower intrinsic luminosity, so it has to be closer with a larger parallax. In spite of the uncertainties that plague the spectroscopic surface gravity determination, we believe that in this case it is more reliable than that derived from the parallax. Since our radial velocity measurements imply that the star is a binary, we expect that its astrometric measurements also contain a component due to the orbital motion. The astrometric data should then be processed using one of the astrometric binary processing pipelines of Gaia (Halbwachs et al. 2023; Holl et al. 2023) that would result in a parallax different from that available in Gaia DR3, which was obtained treating the star as a single star. As mentioned above, the spectroscopic surface gravity implies that this parallax should be larger than that in Gaia DR3. With the adopted parameters ($T_{\text{eff}}=5159$, $\log g=2.1$, $[\text{Fe}/\text{H}]=-1.8$), we derived these possible masses and ages (see Fig. 3):

- $M = 2.3 M_{\odot}$ and age of 493 Ma (3, RGB, red giant branch, or the quick stage of red giant for intermediate+massive stars²);
- $M = 2.3 M_{\odot}$ and age of 504 Ma (4, CHEB, core He-burning for low mass stars, or the very initial stage of CHEB for intermediate+massive stars);
- $M = 1.9 M_{\odot}$ and age of 904 Ma (7, EAGB, the early asymptotic giant branch).

In the most extreme case, with an adopted $\log g$ of 2.5 dex, we derived the following:

- $M = 1.4 M_{\odot}$ and age of 2 Ga (3);
- $M = 0.8 M_{\odot}$ and age of 8.4 Ga (7).

3.4. Kinematics

The fact that the star is a spectroscopic binary implies that the Gaia DR3 parallax may be incorrect. The Gaia DR3 parallax was derived assuming that GHS143 is a single star. The quality of the UVES spectra allowed us to put strong constraints on the

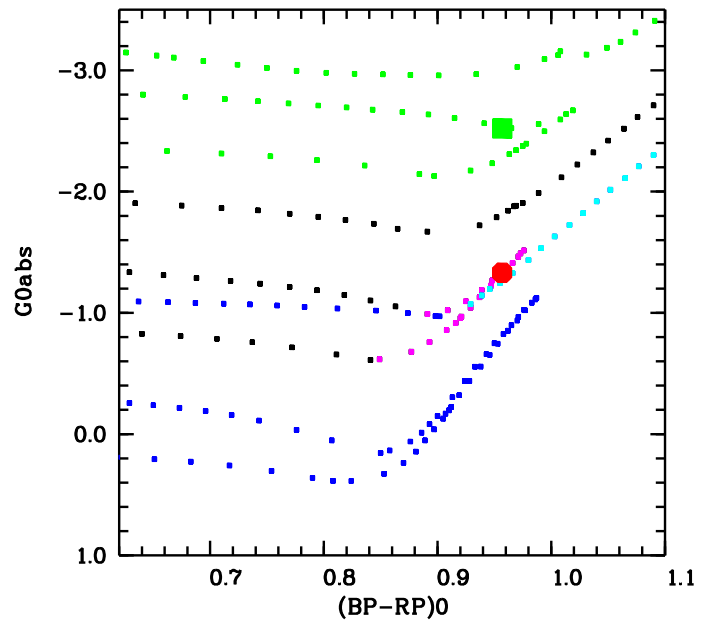


Fig. 3. GHS143 (red circle) in the colour magnitude diagram compared to two isochrones at metallicity -1.65 highlighting the ranges for possible solutions: 500 Ma (black and pink, the evolution stages for the first two solutions) and 1 Ga (dark blue and light blue, the evolution stage for the third solution). The solution with the Gaia DR3 parallax (large green square) adopted in Paper II is compared to the isochrone with an age of 200 Ma (green points).

surface gravity of the star, based on the iron ionisation equilibrium, for which we took into account the NLTE effects. Our preferred gravity is $\log g = 2.1$; taking into account the errors on the Fe I and Fe II abundances, any surface gravity in the interval $1.8 - 2.5$ is consistent with the observations. If we turn around the Stefan–Boltzmann equation and associate a parallax with each surface gravity, this translates into parallaxes from 0.098 mas to 0.222 mas. We investigated how the dynamics of the star changes for various parallaxes in this range. For each parallax we proceeded as in Paper II; we employed the `galpy` code and the MWPotential2014 Galactic potential (Bovy 2015) and the same assumptions on the solar position and motion. For each parallax we considered the astrometric covariance matrix and used the `Pyia` code (Price-Whelan 2018) to produce a random realisation of the stellar kinematic data. For each parallax we extracted 1000 realisations and used them as input to `galpy` to evaluate the dynamical status of the star.

For all parallaxes smaller than 0.168 mas, corresponding to $\log g = 2.24$, the star is unbound, as derived by Bonifacio et al. (2024) from the Gaia DR3 parallax. For a parallax of 0.168 mas the star is partially unbound, in the sense that it is unbound for 609 realisations out of 1000. For larger parallaxes the star becomes bound, albeit with a large apocentre, in excess of 30 kpc with our adopted Galactic potential. We conclude that the boundary between being bound and unbound is around $\log g = 2.2$, higher surface gravities make the star bound, while lower values make it unbound, in the adopted Galactic potential.

3.5. Abundances

The chemical investigation provided in Table A.1 is from the spectrum observed in November 2023. The star is poor in carbon, but rich in nitrogen and oxygen. The C abundance was derived by line profile fitting of the G-band at about 428 nm.

² http://stev.oapd.inaf.it/cmd_3.1/faq.html

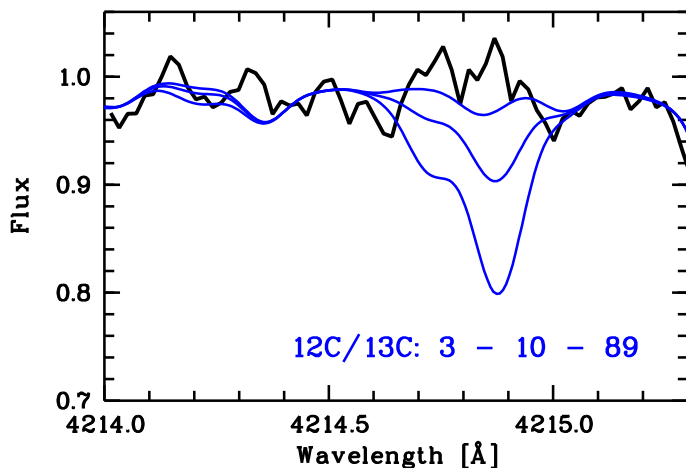


Fig. 4. Observed spectra (solid black) compared to theoretical synthesis in the G-band range where ^{13}C line are expected.

We did not detect any ^{13}C (see Fig. 4), and we concluded that the $^{12}\text{C}/^{13}\text{C}$ is not higher than solar. We investigated the CN band at 383 nm and, fixing the C abundance, we derived N abundance of $A(\text{N})=6.83$. Oxygen was derived from the [OI] line at 630 nm and from the triplet at 777 nm. The lines of the triplet are affected by non-negligible NLTE effects, while the forbidden line forms in conditions close to LTE. By correcting the O abundance for NLTE effects (Sitnova et al. 2013) the four O I lines are in very close agreement, and in this case we derived $[(\text{C}+\text{N}+\text{O})/\text{Fe}]=0.65$.

The star is enhanced in α elements. From ten Mg I lines we derive $[\text{Mg}/\text{Fe}] = +0.52$ (see Fig. A.3). The NLTE corrections for Fe and Mg are comparable (+0.08 dex for the four Mg I lines used here; Bergemann et al. 2017), so the $[\text{Mg}/\text{Fe}]$ ratio, taking into account the NLTE corrections, is close to the LTE value. From 15 lines of Si I we derived $[\text{Si}/\text{Fe}] = +0.46$ and from one Si II line $[\text{Si}/\text{Fe}] = +0.35$. For the four lines the NLTE correction is small (-0.03 dex, Bergemann et al. 2013). From 23 Ca I lines we derived $[\text{Ca}/\text{Fe}] = +0.46$ (see Fig. A.3). Of the Ca I lines investigated, 11 provided a NLTE correction of +0.09 dex (Mashonkina et al. 2007), similar to the NLTE correction of iron.

The $A(\text{Ti})$ is derived from Ti I and Ti II features (23 and 32 lines, respectively), providing an enhancement in $[\text{Ti}/\text{Fe}]$ ($[\text{Ti}/\text{Fe}] = 0.40 \pm 0.17$ and $[\text{Ti}/\text{Fe}] = 0.41 \pm 0.13$, respectively). The Ti abundance derived from the Ti II lines is close to the LTE condition (see Sitnova et al. 2020), so this value should be preferred.

Sodium is derived from four Na I lines (498.2, 616.0, 818.3, and 819.5 nm) and provided $[\text{Na}/\text{Fe}] = 0.13 \pm 0.23$ (see Fig. A.3). According to Takeda et al. (2003) the three reddest lines are affected by NLTE corrections that reduce the Na abundance by about -0.2 dex and decrease the line-to-line scatter. We analysed the strong Al I line at 396 nm. The NLTE correction for this line is 0.6 dex, according to Andrievsky et al. (2008). The K I line at 769.8 nm provided $[\text{K}/\text{H}] = -0.87$ dex, so a strong K enhancement ($[\text{K}/\text{Fe}] = 0.93$ dex). Taking into account the NLTE correction provided by Reggiani et al. (2019), we obtained a NLTE $[\text{K}/\text{Fe}]$ ratio of +0.41 dex, making the star still rich in K, but not so extreme.

We derived abundance values from neutral and single ionised V, Cr, and Mn, and the abundances derived are consistent with that derived from Fe I and Fe II lines: the abundance from ionised lines is higher by about 0.1 dex (in the case of V 0.2 dex) than that from neutral lines. Ni and Co (from 10 and 36 neutral lines,

respectively) provide consistent values with Fe (see Fig. A.3). The Cu I line at 578.2 nm provides a negative $[\text{Cu}/\text{Fe}]$ ratio ($[\text{Cu}/\text{Fe}] = -0.37$ dex), but this is known to be a NLTE effect (see Caffau et al. 2023). The star is slightly enhanced in Zn ($[\text{Zn}/\text{Fe}] = 0.19$ dex) and in Zr ($[\text{Zr}/\text{Fe}] = 0.34$ dex). For Zn, according to Sitnova et al. (2022), the NLTE correction on $A(\text{Zn})$ is 0.16 dex, so taking into account NLTE corrections on both elements, we derive $[\text{Zn}/\text{Fe}] = 0.24$.

We investigated two Sr II (407.7 and 421.5 nm) lines and one Sr I (460.7 nm) to derive the Sr abundance. The NLTE correction of the Sr I is about 0.4 dex according to Bergemann et al. (2012a). We fitted the five Ba II lines (455.4, 493.4, 585.3, 614.1, and 649.6 nm) available in the wavelength range and we derived that the star is slightly enhanced in Ba ($[\text{Ba}/\text{Fe}] = 0.43$) (see Fig. A.3). We verified that the partition function for La, Ce, Nd, Sm, Eu, Dy, and Er in SYNTHE was good by computing few lines with Turbospectrum and derived very consistent results. For the heavy elements we investigated the La II, Ce II, Nd II, Sm II, Dy II, and Er II lines. The two Eu II lines (412.9 and 664.5 nm) were fit and they provided $[\text{Eu}/\text{Fe}]=0.25$.

3.6. Uncertainties

The uncertainties in the stellar parameters are related to the uncertainties in the Gaia photometry and astrometry, the way to derive the stellar parameters, and the reddening. In Sect. 3.2, different ways to derive T_{eff} are discussed, each of which brings very consistent values. Had we used the calibration by Mucciarelli et al. (2021) instead of the comparison to synthetic photometry and colour as applied in Paper II, we would have derived a temperature 60 K hotter. We then assume an uncertainty of 100 K in T_{eff} . The microturbulence derived from the Fe I lines provides a value of 1.65 km s^{-1} , while the calibration by Mashonkina et al. (2017) provides a value about 0.2 km s^{-1} higher. We assigned 0.2 km s^{-1} as the uncertainty in microturbulence.

For the surface gravity things are more complicated. The uncertainty in the parallax is of 37%, providing an uncertainty in $\log g$ of 0.2 dex. However, deriving the $\log g$ from the balance of $A(\text{Fe})$ from the Fe I and Fe II lines, we converge to a $\log g$ of 2.1 dex, which is 0.3 dex higher than the value derived from the parallax. With $\log g=1.8$ dex as derived from the Gaia DR3 photometry and parallax corrected by the zero point, we obtained a perfect balance of $A(\text{Fe})$ from the Fe I and Fe II lines in LTE, and the value would still be compatible after applying the NLTE correction within the uncertainties. With $\log g=2.5$ dex we derived $A(\text{Fe}) = -1.81 \pm 0.11$ from the Fe I lines to which we have to add 0.08 dex to take into account NLTE corrections and $A(\text{Fe}) = -1.52 \pm 0.12$ from the Fe II lines. The two values, -1.73 ± 0.11 and -1.52 ± 0.12 dex, are compatible within the uncertainties. We adopted 0.4 dex as the uncertainty in the surface gravity (see Fig. 2).

The uncertainties in the stellar parameters implies uncertainties in the abundances derived, and are provided in Table A.2. To derive the random uncertainties we compared the results of the two UVES spectra.

4. Discussion and conclusions

The analysis of the UVES high-resolution spectra of GHS143 has allowed us to gain further insight into the nature of this star, and also to highlight some difficulties in the interpretation of the data. The first important result is that the star is a single-spectrum spectroscopic binary (SB1), on the basis of the radial velocities measured from the two spectra. As discussed in Sect. 3.4,

the iron ionisation equilibrium allows a range of possible surface gravities. The range $2.2 \leq \log g \leq 2.5$ implies a distance that makes the star bound. The young apparent age and high mass of the star remain true for all but the extreme gravity of $\log g = 2.5$ dex and the assumption that it is on the AGB. Even in this extreme case, however, the age is only 8.4 Ga, which is younger than the bulk of the halo stars. This, coupled with the large apogalacticon distances implied in all cases that make the star bound, makes it more likely that the star formed in an external galaxy and was accreted by the Milky Way.

The abundances derived for this star seem well in line with the typical abundance patterns found in the Milky Way halo for all elements except CNO. The pattern of the CNO abundances is quite exceptional.

A carbon-to-iron ratio $[C/Fe] \approx -0.4$ is compatible with what is observed in some ultra-faint dwarf galaxies such as Boo I (see e.g. Frebel et al. 2016; Norris et al. 2010, and references therein), Segue 1 (Norris et al. 2010), Uma II, and Coma Ber (Frebel et al. 2010), and also in the Milky Way halo (see e.g. Barklem et al. 2005). However, a carbon-to-oxygen ratio $[C/O] = -1.2$ is far lower than what is observed in Milky Way stars (Akerman et al. 2004; Spite et al. 2005). There are unfortunately not enough oxygen measurements in dwarf galaxies to say much about the C/O ratio. The ratio $[(C+N+O)/Fe] = +0.65$ is very high and quite exceptional. While it may be tempting to interpret the low $[C/O]$ ratio, coupled with the high $[N/O] = -0.03$, as the result of CNO processing, this is not possible in view of the robustly established high $^{12}C/^{13}C$ ratio. The N/O ratio observed in this star is compatible with the ratio observed in Galactic H II regions at galactocentric distances of 10–14 Kpc (Arellano-Córdova et al. 2021), although both the nitrogen and oxygen abundances are almost 1 dex lower. We propose that GHS143, whether bound or unbound, was formed in an external galaxy. We think that the peculiar CNO abundance pattern of GHS143 is a specific signature of this galaxy, although we cannot point to any example of a galaxy with such a chemical pattern.

Acknowledgements. The authors wish to thank the referee. We gratefully acknowledge support from the French National Research Agency (ANR) funded projects “Pristine” (ANR-18-CE31-0017). This work has made use of data from the European Space Agency (ESA) mission *Gaia* (<https://www.cosmos.esa.int/gaia>), processed by the *Gaia* Data Processing and Analysis Consortium (DPAC, <https://www.cosmos.esa.int/web/gaia/dpac/consortium>). Funding for the DPAC has been provided by national institutions, in particular the institutions participating in the *Gaia* Multilateral Agreement. This research has made use of the SIMBAD database, operated at CDS, Strasbourg, France.

References

- Akerman, C. J., Carigi, L., Nissen, P. E., Pettini, M., & Asplund, M. 2004, *A&A*, 414, 931
- Amarsi, A. M., Lind, K., Asplund, M., Barklem, P. S., & Collet, R. 2016, *MNRAS*, 463, 1518
- Andrievsky, S. M., Spite, M., Korotin, S. A., et al. 2008, *A&A*, 481, 481
- Arellano-Córdova, K. Z., Esteban, C., García-Rojas, J., & Méndez-Delgado, J. E. 2021, *MNRAS*, 502, 225
- Barklem, P. S., Christlieb, N., Beers, T. C., et al. 2005, *A&A*, 439, 129
- Bergemann, M., Collet, R., Amarsi, A. M., et al. 2017, *ApJ*, 847, 15
- Bergemann, M., Hansen, C. J., Bautista, M., & Ruchti, G. 2012a, *A&A*, 546, A90
- Bergemann, M., Kudritzki, R.-P., Würl, M., et al. 2013, *ApJ*, 764, 115
- Bergemann, M., Lind, K., Collet, R., Magic, Z., & Asplund, M. 2012b, *MNRAS*, 427, 27
- Bonifacio, P., Caffau, E., Monaco, L., et al. 2024, *A&A*, in press
- Bovy, J. 2015, *ApJS*, 216, 29
- Caffau, E., Bonifacio, P., Sbordone, L., et al. 2020a, *MNRAS*, 493, 4677
- Caffau, E., Lombardo, L., Mashonkina, L., et al. 2023, *MNRAS*, 518, 3796
- Caffau, E., Monaco, L., Bonifacio, P., et al. 2020b, *A&A*, 638, A122

- Cayrel, R., Depagne, E., Spite, M., et al. 2004, *A&A*, 416, 1117
- Cescutti, G., Bonifacio, P., Caffau, E., et al. 2022, *A&A*, 668, A168
- Dekker, H., D’Odorico, S., Kaufer, A., Delabre, B., & Kotzlowski, H. 2000, in Society of Photo-Optical Instrumentation Engineers (SPIE) Conference Series, Vol. 4008, Optical and IR Telescope Instrumentation and Detectors, ed. M. Iye & A. F. Moorwood, 534–545
- Frebel, A., Casey, A. R., Jacobson, H. R., & Yu, Q. 2013, *ApJ*, 769, 57
- Frebel, A., Norris, J. E., Gilmore, G., & Wyse, R. F. G. 2016, *ApJ*, 826, 110
- Frebel, A., Simon, J. D., Geha, M., & Willman, B. 2010, *ApJ*, 708, 560
- Gaia Collaboration, Brown, A. G. A., Vallenari, A., et al. 2018, *A&A*, 616, A1
- Gaia Collaboration, Vallenari, A., Brown, A. G. A., et al. 2022, arXiv e-prints, arXiv:2208.00211
- González Hernández, J. I. & Bonifacio, P. 2009, *A&A*, 497, 497
- Halbwachs, J.-L., Pourbaix, D., Arenou, F., et al. 2023, *A&A*, 674, A9
- Holl, B., Sozzetti, A., Sahlmann, J., et al. 2023, *A&A*, 674, A10
- Lindgren, L., Bastian, U., Biermann, M., et al. 2021, *A&A*, 649, A4
- Mashonkina, L., Jablonka, P., Pakhomov, Y., Sitnova, T., & North, P. 2017, *A&A*, 604, A129
- Mashonkina, L., Korn, A. J., & Przybilla, N. 2007, *A&A*, 461, 261
- Mucciarelli, A., Bellazzini, M., & Massari, D. 2021, *A&A*, 653, A90
- Mucciarelli, A. & Bonifacio, P. 2020, *A&A*, 640, A87
- Norris, J. E., Wyse, R. F. G., Gilmore, G., et al. 2010, *ApJ*, 723, 1632
- Price-Whelan, A. 2018, *Adm/Pyia*: V0.2
- Reggiani, H., Amarsi, A. M., Lind, K., et al. 2019, *A&A*, 627, A177
- Roederer, I. U., Preston, G. W., Thompson, I. B., et al. 2014, *AJ*, 147, 136
- Sitnova, T. M., Mashonkina, L. I., & Ryabchikova, T. A. 2013, *Astronomy Letters*, 39, 126
- Sitnova, T. M., Yakovleva, S. A., Belyaev, A. K., & Mashonkina, L. I. 2020, *Astronomy Letters*, 46, 120
- Sitnova, T. M., Yakovleva, S. A., Belyaev, A. K., & Mashonkina, L. I. 2022, *MNRAS*, 515, 1510
- Spite, M., Cayrel, R., Plez, B., et al. 2005, *A&A*, 430, 655
- Suda, T., Hidaka, J., Aoki, W., et al. 2017, *PASJ*, 69, 76
- Suda, T., Katsuta, Y., Yamada, S., et al. 2008, *PASJ*, 60, 1159
- Takeda, Y., Zhao, G., Takada-Hidai, M., et al. 2003, *Chinese J. Astron. Astrophys.*, 3, 316

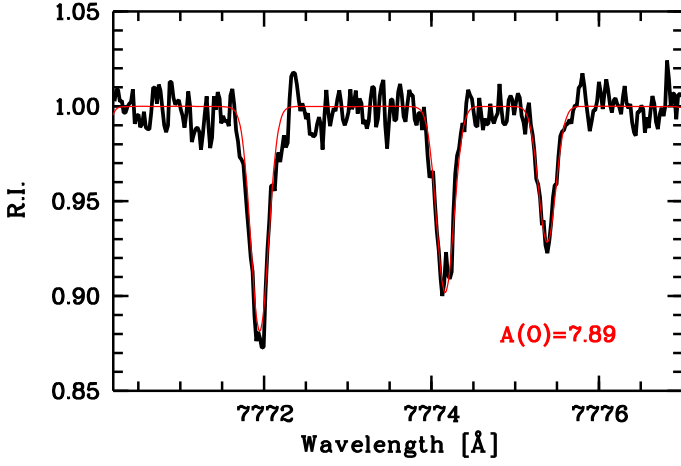


Fig. A.1. O I triplet in the observed spectrum of November 2023 (solid black) compared to a synthesis (solid red) with $A(O)$ value average from the O I triplet lines.

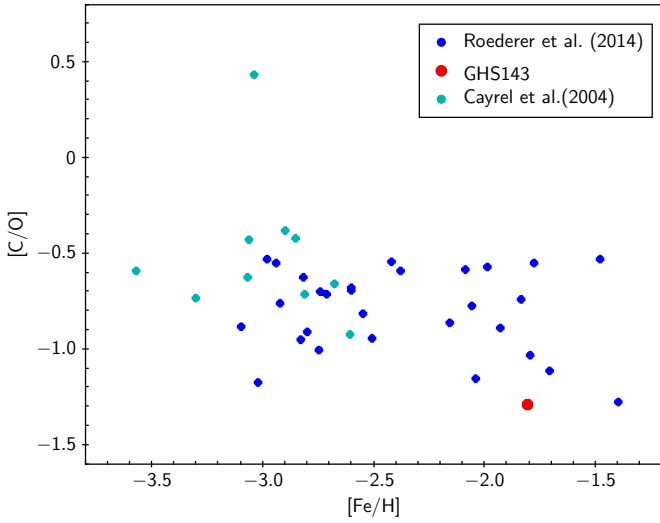


Fig. A.2. $[C/O]$ vs $[Fe/H]$ for GHS143 (blue dot), compared to the unmixed stars from Cayrel et al. (2004, cyan dots) and Roederer et al. (2014, red dots).

Appendix A: Abundances

In Table A.1 the abundances derived from the UVES spectrum observed on November 2023 are listed. In Table A.2 the uncertainties are reported. The second column reports the random uncertainty related to the S/N, derived as the difference between the abundances derived from the two UVES spectra, and the retained lines.

In Fig. A.1 the oxygen triplet is shown. In Fig. A.2 $[C/O]$ vs $[Fe/H]$ of GHS143 is compared to the values of the unmixed stars of the sample of Cayrel et al. (2004), and the stars in Roederer et al. (2014) characterised by a $[C/O] < -0.5$ that are surely unmixed because dwarf, turn-off, and sub-giant stars. As one can see, GHS143 is not alone, but still quite exceptional. In Fig. A.3 the $[X/Fe]$ vs $[Fe/H]$ plots for Na, Mg, Ni and Ba are shown.

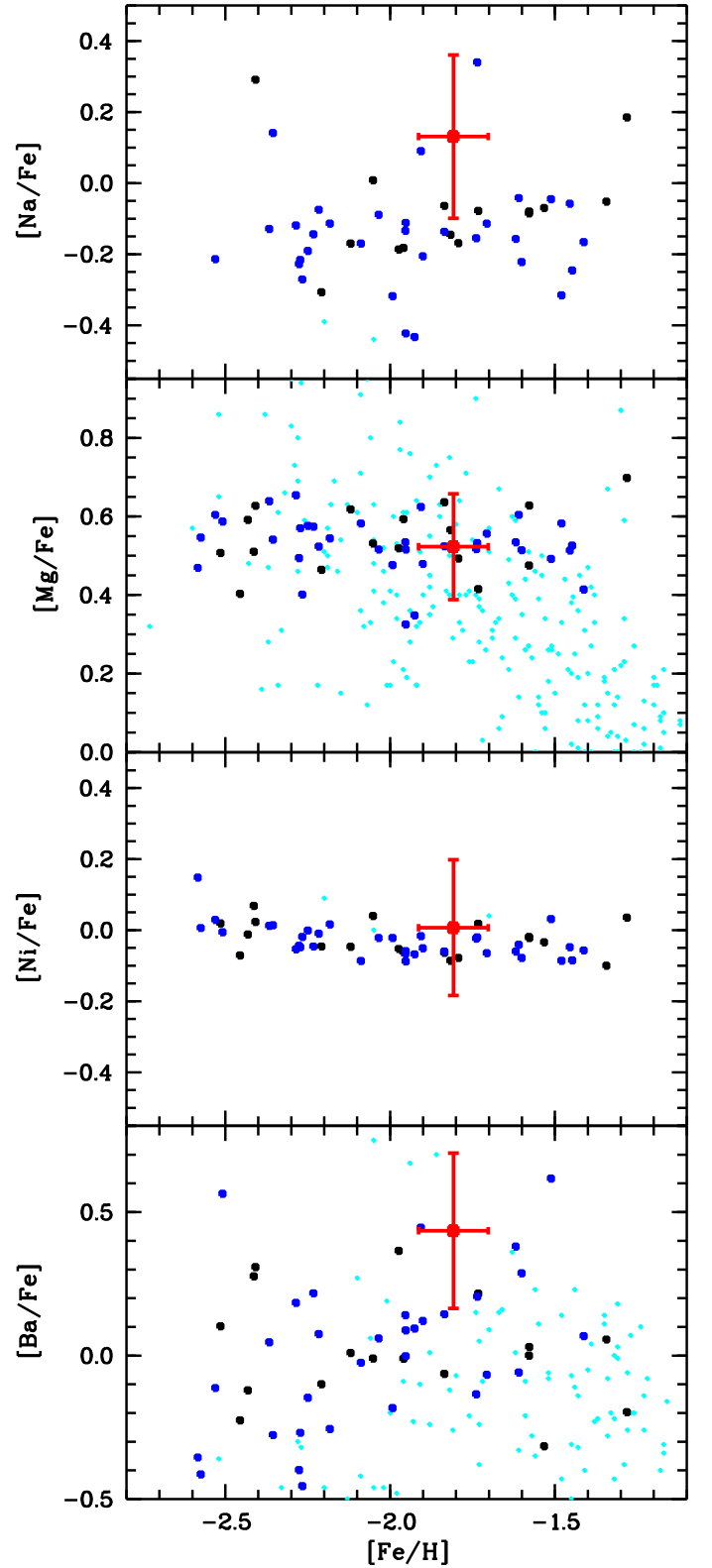


Fig. A.3. $[X/Fe]$ vs $[Fe/H]$ for Na, Mg, Ni, and Ba for GHS143 (red dots), compared to the sample from Caffau et al. (2023, blue dots) and Cescutti et al. (2022, black dots), and from stars from the Sculptor dwarf galaxy taken from the SAGA database (Suda et al. 2008, 2017, light blue dots).

Table A.1. Abundances.

Element	N _{lin}	A(X) _⊙	A(X)	[X/H]	σ	[X/Fe]	σ	Cor(NLTE)
C I	1	8.50	6.300	-2.200	0.100	-0.390	0.145	
N I	1	7.86	6.831	-1.029	0.100	0.779	0.145	
O I	4	8.76	7.849	-0.911	0.085	0.897	0.135	-0.11
Na I	4	6.30	4.623	-1.677	0.204	0.131	0.230	-0.20
Mg I	10	7.54	6.255	-1.285	0.084	0.523	0.135	0.08
Al I	1	6.47	4.311	-2.159		-0.351		0.65
Si I	15	7.52	6.170	-1.350	0.089	0.458	0.138	-0.03
Si II	1	7.52	6.171	-1.349		0.354		
K I	1	5.11	4.236	-0.874		0.934		0.37
Ca I	23	6.33	4.994	-1.336	0.112	0.473	0.154	0.09
Sc I	1	3.10	1.261	-1.839		-0.030		
Sc II	4	3.10	1.517	-1.583	0.061	0.226	0.122	
Ti I	23	4.90	3.490	-1.410	0.135	0.398	0.171	
Ti II	32	4.90	3.604	-1.296	0.080	0.407	0.135	
V I	9	4.00	2.221	-1.779	0.137	0.029	0.173	
V II	5	4.00	2.454	-1.546	0.084	0.157	0.137	
Cr I	16	5.64	3.810	-1.830	0.106	-0.022	0.149	
Cr II	4	5.64	3.898	-1.742	0.120	-0.040	0.161	
Mn I	13	5.37	3.214	-2.156	0.047	-0.347	0.116	
Mn II	1	5.37	3.352	-2.018		-0.315		
Fe I	244	7.52	5.712	-1.808	0.106	0.000		0.11
Fe II	23	7.52	5.817	-1.703	0.108	0.000		
Co I	10	4.92	3.150	-1.770	0.145	0.039	0.180	
Ni I	36	6.23	4.429	-1.801	0.159	0.007	0.191	
Cu I	1	4.21	2.030	-2.180		-0.371		
Zn I	2	4.62	3.004	-1.616	0.005	0.192	0.106	
Sr I	1	2.92	1.043	-1.877		-0.069		0.4
Sr II	2	2.92	1.476	-1.444	0.078	0.259	0.134	
Y II	9	2.21	0.475	-1.735	0.145	-0.032	0.181	
Zr II	9	2.62	1.237	-1.383	0.136	0.320	0.174	
Ba II	5	2.17	0.893	-1.277	0.248	0.435	0.270	
La II	10	1.14	-0.524	-1.664	0.076	0.039	0.132	
Ce II	10	1.61	-0.145	-1.755	0.079	-0.052	0.134	
Nd II	21	1.45	-0.261	-1.711	0.134	-0.008	0.172	
Sm II	6	1.00	-0.461	-1.461	0.099	0.242	0.146	
Eu II	2	0.52	-0.935	-1.455	0.005	0.248	0.109	
Dy II	1	1.13	-0.405	-1.535		0.168		
Er II	1	0.96	-0.847	-1.807		-0.104		

Table A.2. Uncertainties on [X/Fe].

Ellement	[X/H]	Nlines	T_{eff}	$\log g$	ξ
	random		$\pm 100 \text{ K}$	$\pm 0.4 \text{ dex}$	$\pm 0.2 \text{ kms}^{-1}$
Fe I	0.00	244/254	0.10	0.01	0.03
Fe II	0.00	23/22	0.01	0.18	0.04
C I	0.01	G-band	0.08	0.11	0.00
O I	0.03	4/4	0.17	0.18	0.02
Na I	0.03	4/4	0.04	0.00	0.01
Mg I	0.05	8/10	0.04	0.05	0.00
Al I	0.02	1/1	0.10	0.15	0.00
Si I	0.01	15/12	0.06	0.02	0.03
Si II	0.02	1/1	0.01	0.09	0.02
K I	0.05	1/1	0.00	0.08	0.04
Ca I	0.01	26/23	0.02	0.00	0.01
Sc I	0.11	1/1	0.04	0.01	0.02
Sc II	0.02	4/3	0.06	0.10	0.00
Ti I	0.02	23/28	0.00	0.01	0.01
Ti II	0.00	32/35	0.04	0.01	0.01
V I	0.01	9/8	0.05	0.01	0.02
V II	0.04	5/4	0.04	0.06	0.00
Cr I	0.01	16/14	0.00	0.00	0.02
Cr II	0.02	4/4	0.01	0.02	0.02
Mn I	0.02	13/15	0.01	0.01	0.01
Mn II	0.04	1/1	0.08	0.10	0.03
Co I	0.04	10/9	0.03	0.00	0.01
Ni I	0.02	36/32	0.01	0.00	0.02
Cu I		1/0	0.06	0.00	0.03
Zn I	0.04	2/2	0.06	0.08	0.01
Sr II	0.04	2/2	0.10	0.15	0.00
Y II	0.03	9/11	0.06	0.01	0.02
Zr II	0.01	9/9	0.07	0.06	0.00
Ba II	0.04	5/3	0.06	0.02	0.11
La II	0.04	10/10	0.07	0.02	0.03
Ce II	0.02	11/15	0.07	0.05	0.04
Nd II	0.02	21/21	0.05	0.06	0.03
Sm II	0.10	7/6	0.07	0.01	0.04
Eu II	0.08	2/2	0.04	0.04	0.04
Dy II	0.03	1/1	0.09	0.07	0.06
Er II	0.07	1/1	0.06	0.01	0.03